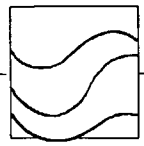

Stratified flow
Rotating flow
Fronts
Buoyancy

A laboratory study of buoyant fresh water boundary currents in tidal crossflows

Peter A. DAVIES, Pieter T.G.A. JACOBS, Linus A. MOFOR

Department of Civil Engineering, The University, Dundee DD1 4HN, UK.

ABSTRACT

Laboratory modelling experiments have been conducted to simulate the behaviour and stability characteristics of a buoyant boundary current formed by the discharge of river water into a tidal crossflow. Results from parametric studies of conditions typical of the Channel are presented to show: a) the different forms taken by the boundary currents for stable and unstable currents respectively; b) the dependence of the nose velocity and current width of the boundary current upon the driving density difference and the amplitude of the tidal forcing; and c) variation with Burger number Bu of the growth rate and wavelength of the meander-like instabilities. Measurements are also presented to show the spatial and temporal development of the boundary current depth, for a range of external forcing conditions.

The boundary current is shown to develop in three stages, in the first of which the nose moves with the appropriate constant gravity current speed. The second stage is characterised by a decay with time t and along-shore distance x of the nose velocity $u_N(x,t)$ as frictional stresses assume importance. Scaling arguments are advanced to predict a decay with $t^{-1/4}$ and $x^{-1/4}$ for u_N, and the results show fair agreement with this prediction. In the final stage of development the driving buoyancy pressure gradient is weak and the nose velocity is controlled principally by the tidal forcing. The data show that the spatially-averaged nose velocity, scaled with the gravity current velocity: 1) increases with increasing Rossby number Ro; and 2) decreases with increasing Burger number.

The mean width λ (x_0 ,t) of the boundary current at a given along-shore reference station x_0 is shown to increase with time as predicted by simple scaling considerations, but there is significant quantitative discrepancy in the growth rate; the much stronger lateral growth than predicted is ascribed to deficiencies in the viscous dissipation model and neglect of interfacial mixing. No dependence on Bu is found for the growth rate of the current width λ (x_0, t) which varied roughly from 0.6 to 4.0 times the internal Rossby radius of deformation R_d. The time-averaged boundary current width, scaled with R_d, is shown to decrease with increasing Bu and Ro, and the boundary current depth h (x_0 ,y_0 ,t) at a fixed along-shore location (x_0 ,y_0), is shown to increase with time at a rate which decreases with increasing Bu.

The amplitudes of boundary current instabilities are found to decrease with increasing Bu only for high values of Ro. In these cases, the instabilities are judged to be barotropic. The wavelengths of the unstable flows, scaled with R_d, appear to decrease with increasing Bu and with decreasing Ro. Agreement is found with measurements made by Griffiths and Linden [1982] for the ratio of wavelength and boundary current width at high Ro.

Oceanologica Acta, 1993, **16**, 5-6, 489-503.

RÉSUMÉ

Étude en laboratoire de courants d'eau douce traversant des flux de marée

Des expériences de laboratoire ont été effectuées pour simuler les caractéristiques du comportement et de la stabilité d'un courant de densité lorsqu'un écoulement de marée est traversé par un courant d'eau en provenance d'une rivière. Les résultats obtenus avec des paramètres caractéristiques de la Manche montrent : a) les formes différentes prises par les courants de densité dans les cas de stabilité et d'instabilité ; b) la vitesse du nez du front et la largeur du courant en fonction de l'écart de densité entre les deux eaux et de l'amplitude des courants de marée ; c) l'effet du nombre de Burger, Bu, sur le taux de croissance et la longueur d'onde des instabilités de type méandre. Les mesures montrent aussi le développement spatial et temporel de la profondeur du courant, pour toute une gamme de conditions de forçage externes.

Le courant de densité se développe en trois phases. Dans la première, la vitesse du nez est celle du courant de gravité. La deuxième phase est caractérisée par une diminution de la vitesse du nez $u_N(x, t)$ avec le temps t et avec la distance x le long de la côte, les forces de frottement devenant significatives.

Des considérations d'échelle sont proposées : elles prévoient une diminution en $t^{-1/4}$ et $x^{-1/4}$ pour u_N. Les résultats sont en bon accord avec la prévision. Dans la phase finale du développement, le gradient de pression déterminant l'équilibre des eaux est faible et la vitesse du nez est contrôlée principalement par le forçage de la marée. Ces données montrent que la moyenne spatiale de la vitesse du nez adimensionnalisée par la vitesse du courant de gravité : a) augmente avec le nombre de Rossby, Ro ; et b) diminue lorsque le nombre de Burger, Bu, augmente.

La largeur moyenne $\lambda(x_0, t)$ du courant de densité côtier, à un x_0 donné, augmente avec le temps, comme prévu par de simples considérations d'échelle, mais il y a un désaccord significatif sur la valeur du taux de développement ; la croissance latérale beaucoup plus forte que prévu est attribuée aux défauts du modèle de dissipation visqueuse, et qui néglige le mélange à l'interface. Aucun effet du nombre de Burger n'a été trouvé sur la variation de la largeur du courant $\lambda(x_0, t)$, qui est de l'ordre de 0,6 à 4,0 fois le rayon de déformation interne de Rossby, R_d. La moyenne temporelle de la largeur du courant, pour R_d fixe, diminue lorsque Bu et Ro augmentent, et la profondeur du courant limite $h(x_0, y_0, t)$ en un endroit (x_0, y_0) le long de la côte augmente avec le temps à une vitesse qui diminue lorsque Bu augmente.

Les amplitudes des instabilités du courant diminuent lorsque Bu augmente, uniquement pour les valeurs élevées de Ro. Dans ce cas, les instabilités sont barotropes. Les longueurs d'onde des écoulements instables, adimensionnalisées par Rd, diminuent lorsque Bu augmente et lorsque Ro diminue. Les résultats de Griffiths et Linden (1982) sont en bon accord en ce qui concerne le rapport de la longueur d'onde avec la largeur du courant lorsque Ro est élevé.

Oceanologica Acta, 1993, **16**, 5-6, 489-503.

INTRODUCTION

This paper describes the results of a laboratory modelling study of coastal front formation in a tidal environment. The study was motivated by questions concerning the motion of fresh and/or brackish water discharged from the Seine and Somme rivers into the English Channel and the consequent formation of salinity fronts and buoyant boundary currents along the French coast. Parametric laboratory investigations have been conducted: a) to determine conditions under which fronts form; and b) to measure the spatial and temporal structures of the associated boundary currents.

Evidence for the formation of coastal fronts in the eastern English channel has come most recently from high resolution, multispectral airborne thematic mapper (ATM) data from remote sensing aircraft overflights of the Cap Gris-Nez region (Matthews and Boxall, 1991) and field observations (Brylinski and Lagadeuc, 1990). The nature of the remote sensing data and the evidence of the field measurements suggest that fronts in the Channel may be associated with horizontal gradients in salinity, temperature and turbidity and that these fronts occur typically between 2 and 10 km from the French coast. In the cases studied by Brylinski and Lagadeuc (1990) for the

spring and summer fluvial input from the coastal strip extending from the Bay of Seine to Cap Gris-Nez, the front was found to be essentially salinity-controlled, with thermal gradients playing a relatively weak rôle in the localisation of the front. River plume fronts of this type have been known for some time to occur in coastal waters as a result of salinity differences between the river outflow and the saline tidal cross flow and many field experiments have been performed to investigate their characteristic features, for shallow and deep water coastal conditions (Kao, 1981; Garvine, 1981; Chao, 1988). In all cases, the effect of the Earth's background rotation is to restrain the buoyant river inflow against the coast to the right (in the northern hemisphere) of the inlet (Griffiths, 1986).

In contrast to the salinity fronts observed by Brylinski and Lagadeuc (1990), the remote sensing data from summer overflights of the same region (Matthews and Boxall, 1991) showed evidence in the thermal infrared channels for strong frontal thermal gradients. Accompanying discontinuities in suspended sediment distributions were inferred from the visible channels data. In order to explain such characteristics, appeal may be made to the tidal stirring mechanism (Simpson and James, 1986) recognised as being of controlling importance for the formation of shelf sea fronts. That such a mechanism can operate in the coastal context is clear for cases in which river inflows are weak or absent and for which offshore thermally-stratified summer conditions obtain. For these circumstances, the reduction in water depth H towards the coast and the associated relative increase in bottom friction both conspire to enhance vertical mixing and reduce the local value of H/U^3 to below its threshold level for stratified conditions to be maintained. However, in contrast to the cases of offshore shelf fronts (Pingree and Griffiths, 1978; Simpson, 1981), the locations of the tidally-stirred fronts in shallow coastal regions are relatively difficult to predict with acceptable precision because of a) the uncertainty limits on the critical value (~ 500) of the H/U^3 parameter for frontal formation; and b) the sensitivity of the formation criterion (Simpson and James, 1986):

$[\log_{10}(H/U^3)]_{crit} = 2.7$

to uncertainties in U, the depth mean tidal velocity (averaged over a tidal cycle) in the nearshore waters. Thus far, numerical models of the Pas-de-Calais are unable to contribute to a resolution of this positional uncertainty because of their inability to accommodate the subgrid scale three-dimensional density field processes occurring in the frontal region.

The evidence outlined above confirms that river plume and tidal stirring effects may both contribute to frontal formation along the French Channel coast, though the operation of either of the two causal mechanisms in the presence of the other is not clear. In addition, questions remain as to a) the relative dominance and respective horizontal length scales of each of the formation mechanisms; and b) the significance of other dissipation processes such as Ekman pumping. In the present paper, the formation of fronts associated specifically with the inflow of fresh or brackish river inflow into nearshore tidal saline waters is considered.

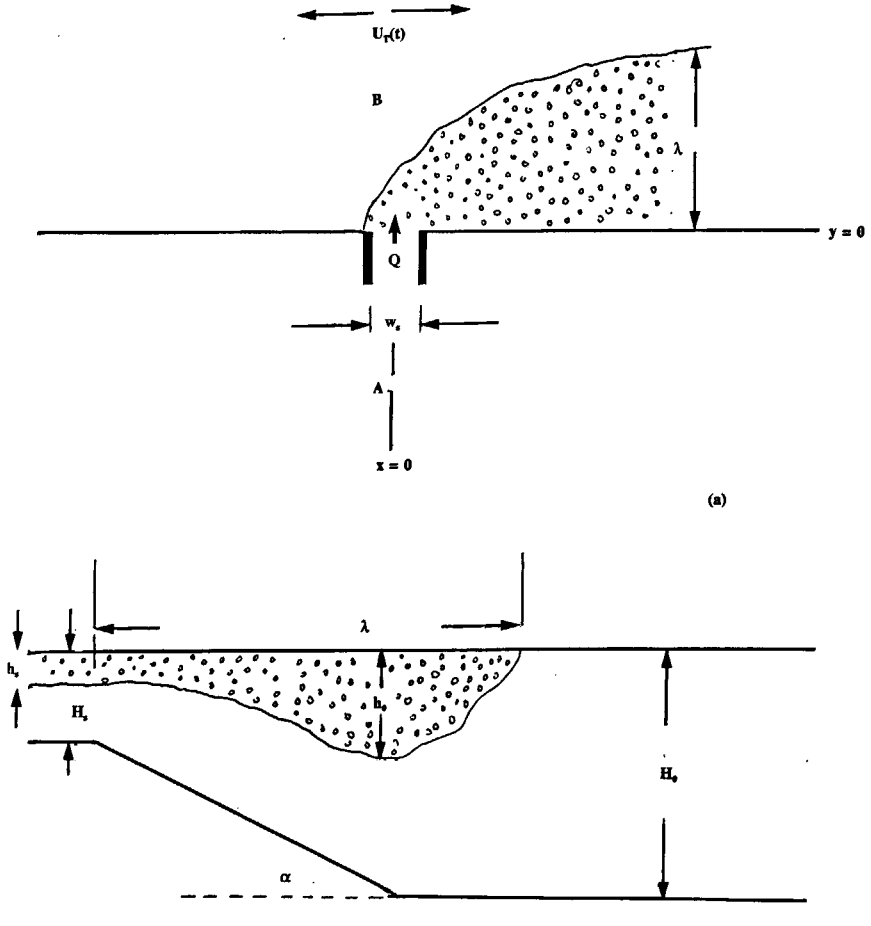

Figure 1

Schematic representation of flow under consideration: a) in plan; and b) side elevation.

PHYSICAL SYSTEM

The system under consideration is illustrated schematically in Figure 1. In a Cartesian system (x, y, z) rotating with uniform angular velocity Ω_0 (= 0, 0, Ω_0), a homogeneous fluid of density ρ_0 and kinematic viscosity ν flows steadily with depth-averaged velocity ($U_T(t)$, 0, 0) and depth H(y). The flow is bounded at y = 0 by a vertical solid wall, except at the source region where fluid of density (ρ_0 - $\Delta\rho$) enters with depth h_s, width w_s and discharge Q in the positive y direction. The depths of the receiving waters at the source and offshore are H_s and H_0 respectively, the shore slopes with angle α away from the coast and the gravitational acceleration is (0, 0-g). The

form of the crossflow velocity $U_T(t)$ is sinusoidal, with amplitude $(U_T)_{max}$ and frequency ω. With such a system (which resembles schematically the Somme/Seine inflows into the English Channel), a convenient set of dimensionless dynamical parameters with which to describe the flow development is the following:

$Ro = (U_T)_{max}/fL$
$Fr = Q/(g'H_s^5)^{1/2}$
$Ek = \nu/fH_0^2$
$Bu = (N/f)^2$
$\Phi = \omega/(f/2)$

where Ro, Fr, Ek and Bu are the Rossby, Froude, Ekman and Burger numbers respectively of the flow and Φ is the tidal frequency ratio. In the above, $f = 2\Omega_0$, L is a typical horizontal length scale of the flow, $g' = g(\Delta\rho/\rho_0)$ is the reduced gravitational acceleration and N is the buoyancy frequency defined here by $N^2 = g'/H_s$ [note that $(Bu)^{1/2} = R_d/H_s$, where $R_d = NH_s/L$ is the Rossby radius of deformation of the flow]. Taken together with the geometrical ratios L/H_s, h_s/H_s w_s/H_s and h_s/H_0 and the offshore bottom slope α, the above set is sufficient to describe the flow. For the case of the English Channel, adopting typical values of $(U_T)_{max}$, $(\Delta\rho/\rho_0)$, Q, L, H_s of 1 $m.s^{-1}$, 4 x 10^{-4}, 10^3 $m^3.s^{-1}$, 5 km and 30 m, and a tidal period of 12.5 hours, estimates of the above dynamical parameters are as follows:

$Ro \sim 2$; $Fr \sim 3$; $Bu \sim 0.5$ and $\phi \sim 0.4$

where the value of Ek remains uncertain by several orders of magnitude because of the difficulties of providing a reliable estimate of the equivalent eddy viscosity ν_E for the coastal flow (see later). Note that the above values imply an estimated value of the Rossby radius of about 3 km.

Theoretical aspects

Figure 2 shows schematically the buoyancy-driven boundary current flow which occurs as a result of the configuration described above. As the relatively-light river/estuarine water enters the Channel, there is a deflection to the right due to the Coriolis force, and, because the velocity vanishes at the coastline, a geostrophic coastal current of depth h (x, y, t) and width λ (x, t) is established (Griffiths, 1986). The nose of the current moves with velocity U_N (x, y, z, t), the strength and direction of which are determined by the values of the above dimensionless parameters. From continuity, the flux Q of fresh water may be estimated as:

$$Q \sim hU\lambda \qquad (1)$$

where U (x, t) is the depth- and width-averaged boundary current velocity in the direction of flow (*i.e.* a typical along-shore velocity scale at any cross-section of the boundary current).

The momentum equations in the rotating frame can be used to estimate the velocity and length scales of the boundary current flow in the absence of the crossflow by assuming that: a) the along-stream velocity u is much greater than the corresponding cross-stream and vertical velocities v and w respectively; b) the friction term ν $(\partial^2u/\partial x^2)$ is negligible compared with ν $(\partial^2u/\partial y^2)$ and ν $(\partial^2u/\partial z^2)$; and c) there is negligible interfacial mixing between the boundary current and the quiescent receiving fluid over which it flows. Under these conditions, the momentum equations take the following form:

$$\partial u/\partial t + u\partial u/\partial x = -(1/\rho_0)\,\partial p/\partial x + \nu[\partial^2u/\partial y^2 + \partial^2u/\partial z^2] \qquad (2\,a)$$

$$2\Omega_0 u = -(1/\rho_0)\partial p/\partial y \qquad (2\,b)$$

$$0 = -(1/\rho_0)\partial p/\partial z + g(\Delta\rho/\rho_0) \qquad (2\,c)$$

For cases in which friction is negligible, the essential balance is between the advective and pressure gradient terms in the x direction. From (2 *a*), this balance may be written as:

$$u\partial u/\partial x \sim (1/\rho_0)\partial p/\partial x \qquad (3)$$

such that if $[u\partial u/\partial x] \sim [(U)^2/X]$ and $[(1/\rho_0)\partial p/\partial x] \sim g(\Delta\rho)(h_0\text{-}h)/\rho_0 X$, the nose velocity scale U_N may be estimated as

$$(U_N)^2 \sim g(\Delta\rho)(h_0)/\rho_0 \qquad (4)$$

the inviscid gravity current velocity. In the above, U and X are typical velocity and along flow length scales respectively and h_0 (*see* Fig. 2) is the boundary current depth close to the source (but within the geostrophically-balanced regime). Now, if $[(1/\rho_0)\partial p/\partial y] \sim [g(\Delta\rho)h_0/\rho_0\lambda_0]$, with λ_0 being the current width corresponding to depth h_0, the geostrophic balance equation (2 *b*) and the continuity equation (1) can be used to give

$$h_0^2 \sim 2\Omega_0 Q\rho_0/g(\Delta\rho) \qquad (5\,a)$$

and

$$\lambda_0 \sim [g(\Delta\rho)Q/8\rho_0(\Omega_0)^3]^{1/4} \qquad (5\,b)$$

and hence, from (4) and (5), the inviscid boundary current nose velocity may be estimated as:

$$(U_N)^2 \sim [g(\Delta\rho)\Omega_0 Q/\rho_0]^{1/2} \qquad (6)$$

This may be regarded as the initial velocity of the nose immediately after the buoyant fluid enters the flow and before the outflow is modified by a) friction; and b) the oscillating crossflow. As such, it is a suitable scale with which to normalise measured flow velocities in the boundary currents, notwithstanding the possibility that flow

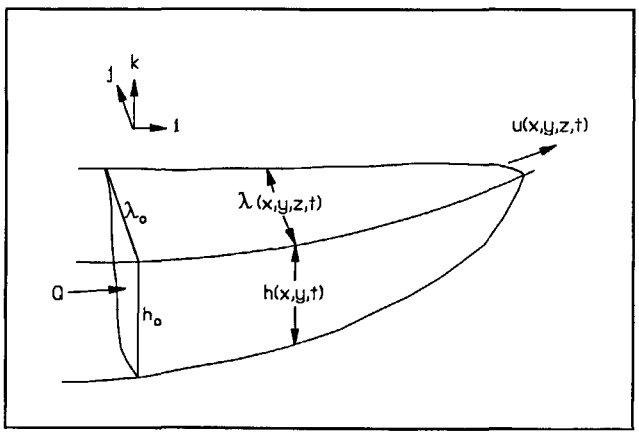

Figure 2

Definition sketch of boundary current.

regimes may exist in which the effects of the two neglected mechanisms (friction, oscillation) may dominate.

Frictional effects assume importance when $(1/\rho_0)\partial p/\partial x \sim \nu(\partial^2 u/\partial y^2) \sim \nu(\partial^2 u/\partial z^2)$ in (2 *a*); by the same reasoning and scaling approach as above, this balance [in conjunction with (1) and (2 *b*)] leads to

$$U_N \sim (1/t)^{1/4}\{[(g')^2 Q h_0/2\Omega_0\nu] - [(Qg')^3/2\Omega_0\nu^2]^{1/2}\}^{1/4} \quad (7)$$

where the additional estimate $U \sim X/t$ has also been used. The above relationships can also be used to obtain the following estimate for the width scale $\lambda_*(t)$ at a reference station $x = x_0$ downstream of the source:

$$\lambda_* \sim (t)^{1/4}\{(\nu g' Q)/[(2g'\Omega_0 h_0) - (8\Omega_0^3 g' Q)^{1/2}]\}^{1/4} \quad (8)$$

Thus, under the assumptions of the above scalings, the velocity of the boundary current decreases as $t^{-1/4}$ while the width at any location x_0 increases with $t^{1/4}$ for a given experiment in which all external quantities are kept fixed. Estimates (6) and (7) and the imposed $\pm (U_T)_{max}$ crossflow forcing scale provide three separate velocity scales for the flow, with each scale being appropriate for different stages of the boundary current development. The crossflow velocity can be expected to dominate in the later stages as the buoyancy pressure gradient weakens and the current has been decelerated by viscous friction.

EXPERIMENTAL APPARATUS

The rotating table facility used for the study consisted of a rotating steel platform upon which was mounted a perspex tank of height $H_0 = 582$ mm and inside radius $R = 455$ mm, filled with salt water of prescribed density. A smooth sloping bottom to the tank was provided by a fixed inverted stainless steel cone of angle α, and a pump was used to supply a regulated prescribed flow of fresh water (dyed with fluorescein) into the working tank, *via* a small rectangular hole. Sponge material placed in front of the hole diffused any initial momentum of the fresh water discharge. The rotating table was driven by a DC motor, itself controlled by a function-generator set to produce a wavelike output rotational speed $\Omega(t)$ of the form

$$\Omega(t) = \Omega_0[1 + \varepsilon \cos(\omega t)]$$

with a modulation amplitude $\Delta\Omega$ $(= \varepsilon\Omega_0)$ and frequency ω superimposed upon a uniform angular velocity Ω_0. With this arrangement, the Rossby number Ro (*see* above) is conveniently expressed as $Ro = \Delta\Omega/\Omega_0$, while the definitions of the other dimensional parameters carry over directly from the definitions presented earlier.

An externally-triggered camera mounted above the tank on the rotating table was used to record sequences of horizontal flow patterns made visible by the fluorescein dye, with the interval between successive frames in the sequence being controlled externally by computer. For the measurements of the vertical structure of the flow, a set of six calibrated aspirating conductivity probes (*see*, for example, Davies *et al.*, 1991) was used to measure the density at a certain depth in the fluid. Each probe could be traversed vertically and individually by means of a calibrated motor and rack arrangement, as shown schematically in Figure 3. A computer mounted on the rotating table was used: 1) to control and/or monitor the vertical positions of the probes; and 2) to log conductivity (and hence density) data from the probes. In the experiments to be described, only the relative density difference and the amplitude of the modulation of the rotational speed have been varied. The values of the dimensionless groups α, H_0/H_s, Φ, Ξ $(= R/H_s)$ and the product (Bu.Fr) were held constant at 30°, 116, 0.4, 9.1 and 0.0066 respectively.

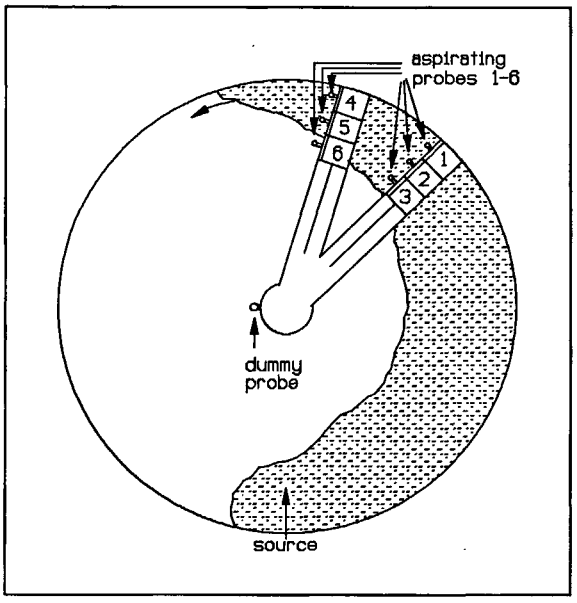

Figure 3

Plan view of probe arrangement for measurement of boundary current structure.

Experimental procedures

For each experiment, fluid of known density was placed in the working tank, and the rotating table was then adjusted to the prescribed value. The fluid was then left to spin up for several hours to a quasi-steady state characterised by a sinusoidal sloshing interior motion superimposed upon quasi-solid body rotation ($\varepsilon = 0$). When this basic state was achieved, the freshwater input discharge was initiated and the synchronised data collection process began by suitable input commands to the computer. The experiment was terminated when the nose and tail of the boundary current met after one circuit of the tank.

For the measurements of the vertical density profiles, the density probes were positioned in such a way that probes 1 and 4, probes 2 and 5 and probes 3 and 6 were paired on the same radial arc (*see* Fig. 3), with each probe being located initially on the surface of the undisturbed fluid. During the experiment, each of the probes was addressed consecutively as the probe in question was moved vertically up and down in small prescribed steps.

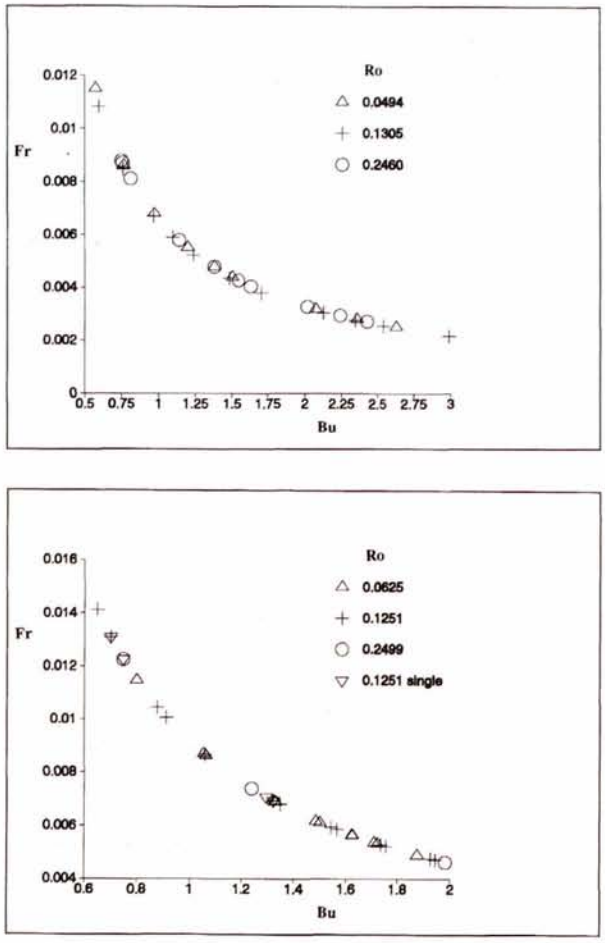

Figure 4

Regime plots showing ranges of experimental parameters for: a) flow visualisation; and b) probe experiments.

Figures 4 *a* and 4 *b* show regime plots of the range of the visualisation experiments and probe experiments respectively. The experiments are divided into three blocks of constant Rossby number Ro (*i.e.* constant amplitude of modulation of the rotational speed) for different fractional density differences. In the cases of the probe experiments, for every set of initial conditions a second experiment was carried out with a different azimuthal position, in order to get twice as many data points. The radial positions of the probes were kept fixed for these experiments on r/R = 0.97, 0.83 and 0.70 for probes 1 + 4, 2 + 5 and 3 + 6 respectively. In the block with Ro = 0.125, four single probe experiments were conducted.

EXPERIMENTAL RESULTS

General features of the flow field

Figure 5 shows two sequences of plan images of the boundary current flow for different external conditions. In both sets, the frontal layer between the boundary current and the undisturbed interior is seen clearly and the current itself is seen to move cyclonically, keeping the wall at its right-hand-side (looking downstream). At

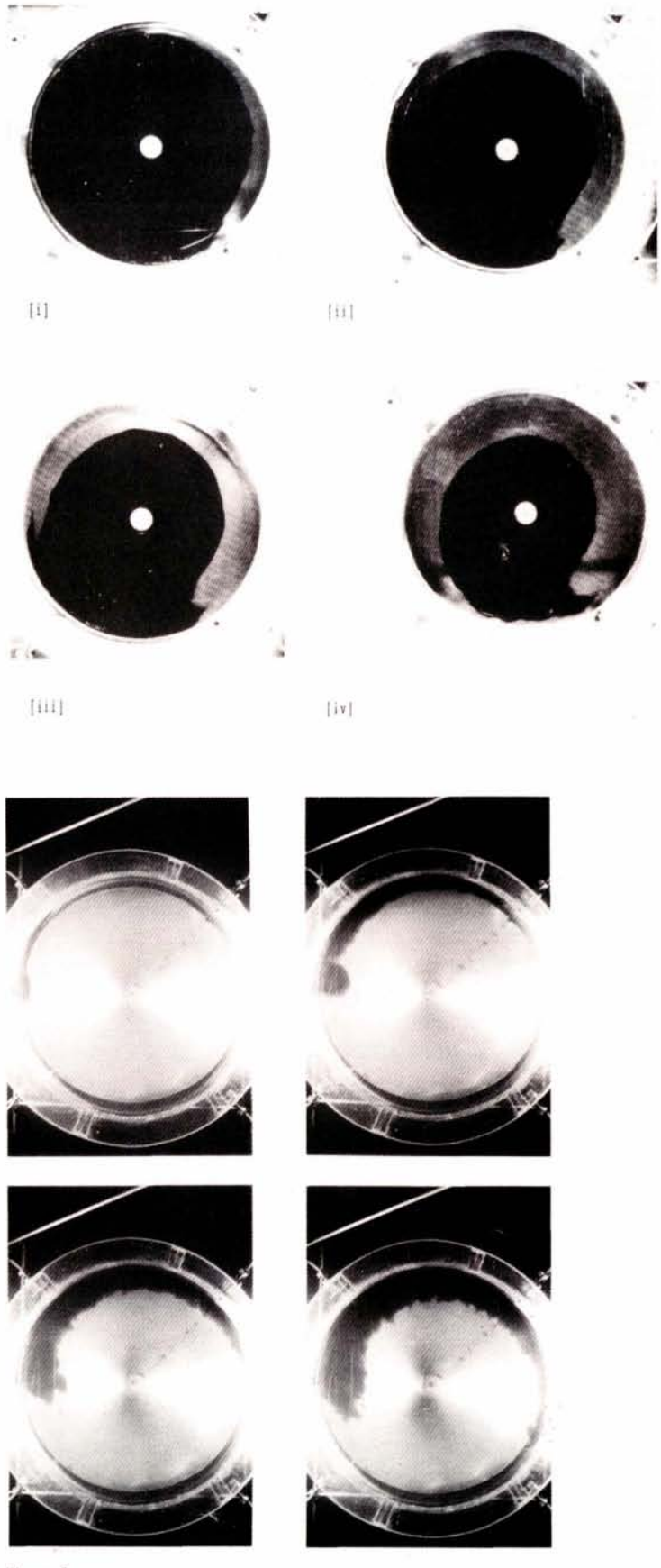

Figure 5

Plan view sequences showing typical boundary current development for: a) stable and (b) unstable flow. Sense of background rotation (a) counterclockwise; and b) clockwise. Parameter values [Bu:Fr:Ro: α:(Δρ/ρ$_0$):Φ: Ξ] = a) [0.035:0.008:0.1:30:0.0023:0.4:9.1]; and b) = [0.18:0.0035:0.033:30:0.0023:0.4:9.1] and dimensionless intervals $\Omega_0 t$ between frames = a) 0.64; and b) 3.8.

the nose of the front the width of the fresh water body decreases gradually to zero.

Various different flow patterns could be identified in the collection of thirty visualisation experiments for changing values of both Ro and Bu. In most of the nine experiments with Ro = 0.0494, disturbances appeared on the boundary between the fresh and the salt water on the free surface. These fronts are classified as unstable (*see*, for example, Fig. 5 *b*). With increasing Burger number, the fronts were initially stable, but subsequently the nose of the current separated from the wall and instabilities began to grow just behind the nose. This happened in all cases, except for one in which (with an intermediate value of Bu), the front was stable throughout the observation period (*see*, for example Fig. 5 *a*). For the experiments with the highest values of Bu, instabilities started to form soon after the initiation of the fresh water supply and the associated disturbances travelled downstream along the front. Sometimes the instabilities had a regular pattern, other times there was no regularity detectable.

In all but one of the experiments with Ro = 0.0494 the front slowed down and came almost to rest downstream from the source. At the same time, a small front separated from the main front and travelled along the wall with a relatively high velocity, leaving the main front behind. Further discussion of this phenomenon is presented below.

For cases with higher values of Ro (for example, the eleven experiments with Ro = 0.1305), there was no evidence for the systematic variation of the flow pattern with increasing Bu seen in the aforementioned experiments. For these cases of relatively high Ro, the classification of stability boundaries was difficult. There were approximately four different flow patterns detectable in this set of experiments: two showed unstable characteristics always (one with small and the other with large amplitude meanders on the frontal interface), but others showed initially a stable flow pattern that was transformed subsequently into an unstable one, regardless of the value of Bu. Finally, some patterns were essentially stable, although vortices were sometimes generated near the source region. For these cases, clear and smooth interfaces were maintained between fresh and salt water bodies. Indeed, in all but one of the experiments with Ro = 0.1305, cyclonic vortices were formed during the first part of the experiment, usually until the nose of the frontal layer reached the stage at which frontal separation from the wall occurred (as for the cases described above).

For the series of experiments with the highest values of Ro (= 0.246), relatively large cyclonic vortices were created continuously at the boundary between the fresh and the salt water. This flow gave rise to a pattern of regular meanders on the frontal interface at the surface and this pattern did not change with changing Bu. In these experiments, in which the modulation of the system caused significant imposed back and forth motion of the current relative to an observer fixed in the uniform rotation (Ω_0) frame, the fresh water input that was then directed to the left at the source formed a tail to the buoyancy current. The tail moved with approximately the same velocity as the nose (but had a much smaller width), so these two parts of the boundary current met eventually at an azimuthal position approximately 180° from the source.

The width of the boundary current varied significantly with Ro and Fr, but was typically between between 2 and 40 % of the radius of the tank. The amplitude of the meanders formed in the cases of unstable flow were typically between 0.3 and 2 % of the path length of the current, and the associated wavelengths of the frontal instabilities in the cases of regular patterns were typically between 2 and 5 % of the path length.

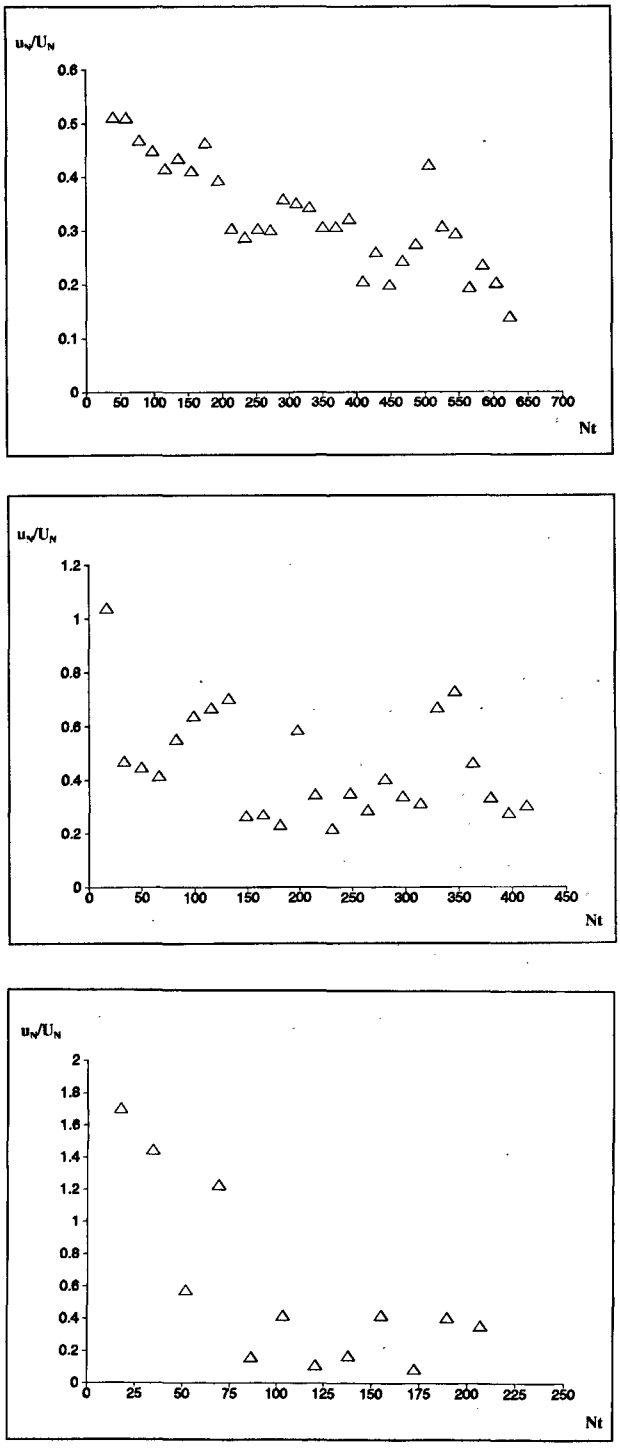

Figure 6

Plots of normalised nose velocity u_N/U_N (see equation 6) versus time Nt for [(Bu)(Fr): α:Φ: Ξ] = [0.0066:30:0.4:9.1] and [$\Delta\rho/\rho_0$):Ro] = a) [0.0022:0.0494]; b) [0.0022:0.1305]; c) [0.0024:0.246].

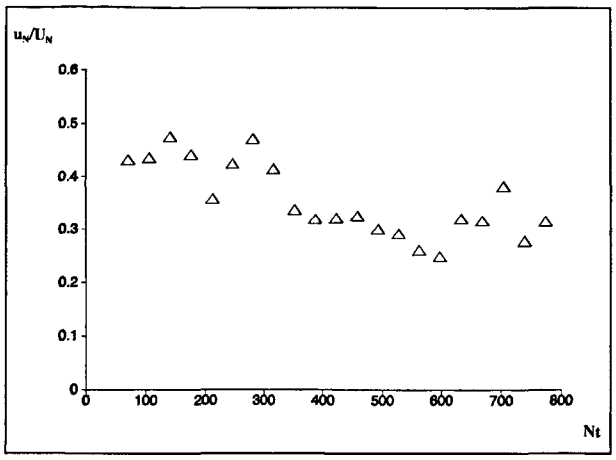

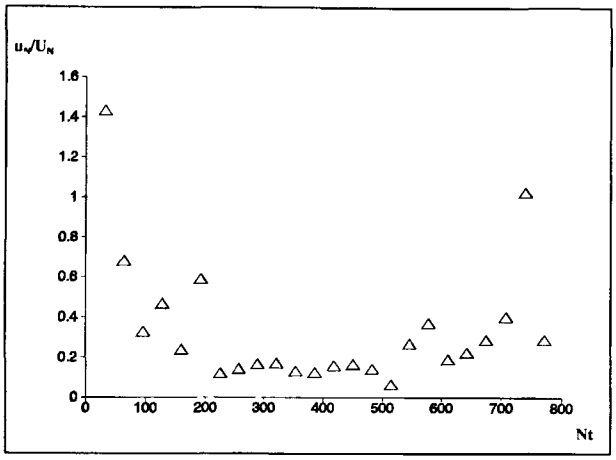

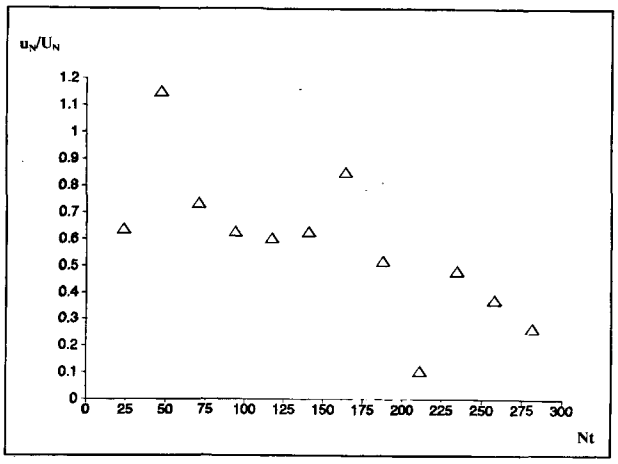

Figure 7

Legend as for Figure 6, except [($\Delta\rho/\rho_0$):Ro] = a) [0.007:0.049]; b) [0.0084:0.131]; c) [0.007:0.246].

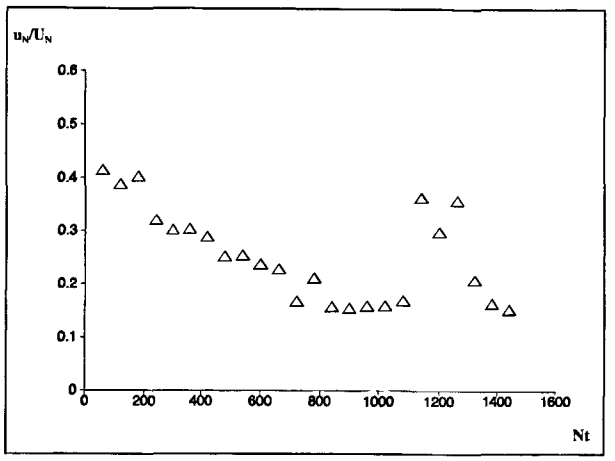

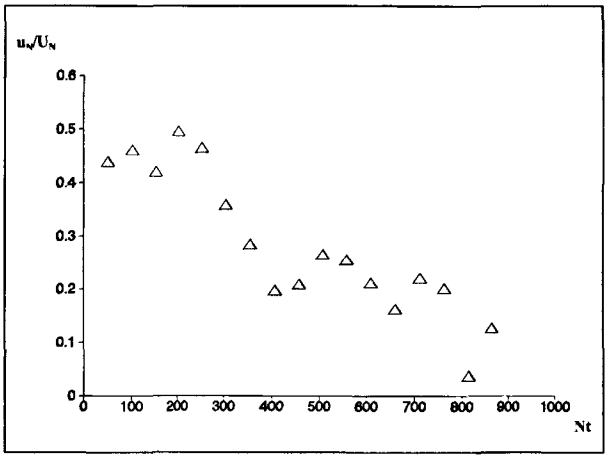

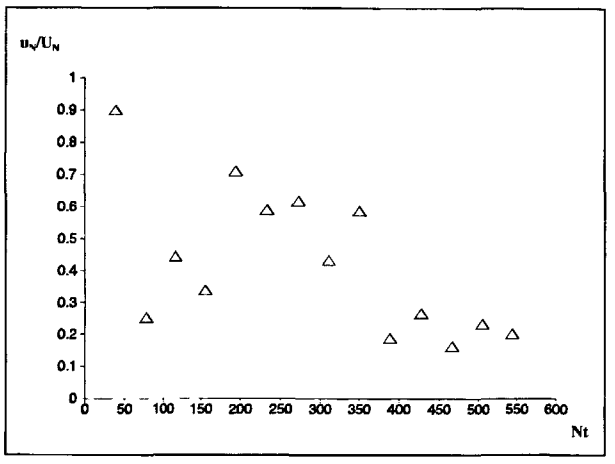

Figure 8

Legend as for Figure 6, except [($\Delta\rho/\rho_0$):Ro] = a) [0.0204:0.049]; b) [0.0211:0.131]; c) [0.0217:0.246].

Measurements of nose velocity, boundary current width and depth and instability characteristics

Each photographic frame of a given experimental sequence was projected on a reference grid and the positions of the nose and lateral boundary of current were marked. In cases of unstable fronts, the surface contour of the free edge of the front was also marked for the whole sequence of frames, and reference marks were added for calibration purposes. A digitising pad linked to a computer was used to measure and store the above dimensions, and the velocity of the nose of the current was then computed from the displacement of the nose between successive frames of known temporal separation.

The change in width of the current with time at the fixed reference station was measured from the marked positions, using the diameter of the tank as a scaling measure. The width was defined as the distance from the vertical wall to the free edge of the boundary current, as identified by the change in dye intensity of the water. In cases of instabilities, the mean width of the boundary current at a given time t was obtained by averaging over a short

reference distance including a maximum and minimum of the edge distortion of the current. The amplitude A of the frontal distortions was measured as the mean difference in radial position between an extremum (maximum or minimum) of an unstable pattern and the mean location of the free edge of the current. The growth rate dA/dt of the instability was determined by monitoring and measuring the increase in the amplitude over a sequence of known time interval. For the calculation of the wavelength κ of the instabilities, the integrated contour of a number of consecutive maxima and minima of the current width on a single frame was drawn, and the length of the contour was measured. Because the width of the boundary current changed over this range, a mean distance from the centre of the tank had to be determined in order to provide an averaged radial position for the wave-like meander on the front. This was done by calculating the radial position for an equal number of maxima and minima, and averaging these positions. Then the length of the contour could be calculated from the averaged radial position and the azimuthal angle covered by the contour. Finally, the wavelength was computed from this length and the number of full periods at the contour.

For the measurement of the depth of the boundary current, the vertical position of the interface between the fresh and salt water was determined for each probe in a given sampling cycle, with this interfacial position being defined as the depth at which the density changed by an arbitrary predetermined amount. The difference between this position and the surface level was then calculated and the depth of the boundary current at each measuring location was determined, using the relevant calibration factors.

Quantitative results

Nose velocity

As described earlier in the "Theoretical aspects" section, a convenient velocity scale with which to normalise the nose velocity measurements is the appropriate gravity current speed $[g(\Delta\rho)\Omega_0 Q/\rho_0]^{1/4}$, *see* (6). Elapsed times may be

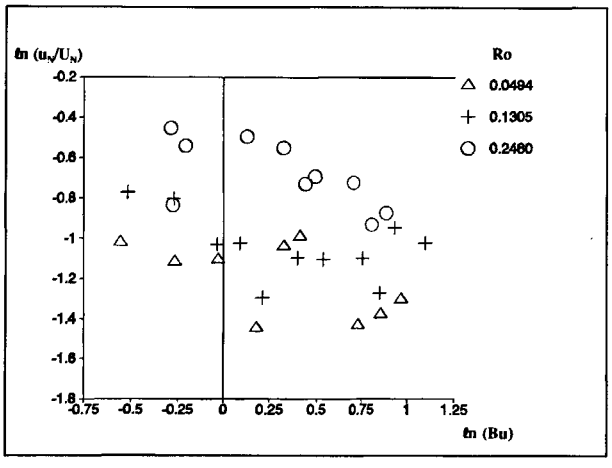

Figure 9

Plot of mean velocity u_m/U_N of nose of boundary current versus *Bu for Ro values shown.*

Table 1

Summary of linear regression fits to velocity-time decay curves (see text).

Ro	Slope	No. of observations
0.049	- 0.38 ± 0.15	9
0.130	- 0.38 ± 0.17	11
0.246	- 0.81 ± 0.31	10

appropriately scaled with the Brunt-Väisälä frequency N, defined earlier as $N^2 = g'/H_s$. Figures 6-8 show the variations with time of the measured nose velocity u_N for low, intermediate and high values of the fractional density difference ($\Delta\rho/\rho_0$) and various values of Ro. As can be seen from these plots, the dimensionless nose velocities generally decay with time in the early stages of motion, though as Ro increases the decreases in the velocity are less smooth. During the initial stage, the dimensionless velocities show some increase with increasing Ro for a given reference time. Figure 9 shows measurements derived from the mean time taken for the front of the current to traverse a known along-shore distance; these data thereby provide a measure of the average nose velocity for given external conditions. For this graph, the average velocity (scaled with gravity current speed) is plotted against the Burger number Bu on a logarithmic scale. It can be seen that the dimensionless nose velocity: a) decreases with increasing Bu for given Ro; and b) increases with increasing Ro for fixed Bu.

The decay in the nose velocity with time is seen on all of the plots of Figures 6-8, at least during the period controlled by the buoyancy driven spread of the boundary current. It is therefore instructive to analyse this time decay with the scaling arguments [*see* estimate (7)] developed in the "Theoretical aspects" section, and this procedure is most conveniently accomplished by a linear regression fit to the data in logarithmic form. By setting empirical limits to the decay phase by inspection of each data set, the slopes of the regression fits have been determined for different fixed values of Ro. The results are summarised in Table 1.

A common feature of the plots of nose velocity *versus* time is the temporary increase in velocity following the initial decay phase. This behaviour is attributed to the modifying effect of the oscillating crossflow upon the relatively weak buoyancy pressure gradient, though a more elaborate discussion of this so-called sloshing effect is presented in a later section.

Boundary current width

The measured boundary current width $\lambda(x_0, t)$ at the reference station $x_0 = \pi R$ from the source is scaled with the width λ_0 derived in equation (5 *b*) in the "Theoretical aspects" section. The normalised width measurements are plotted in Figure 10 against dimensionless time, the latter quantity again being scaled with the Brunt-Väisälä frequency N. In the experiments with Ro = 0.246, the nose of the boundary current mixed with the tail at the reference

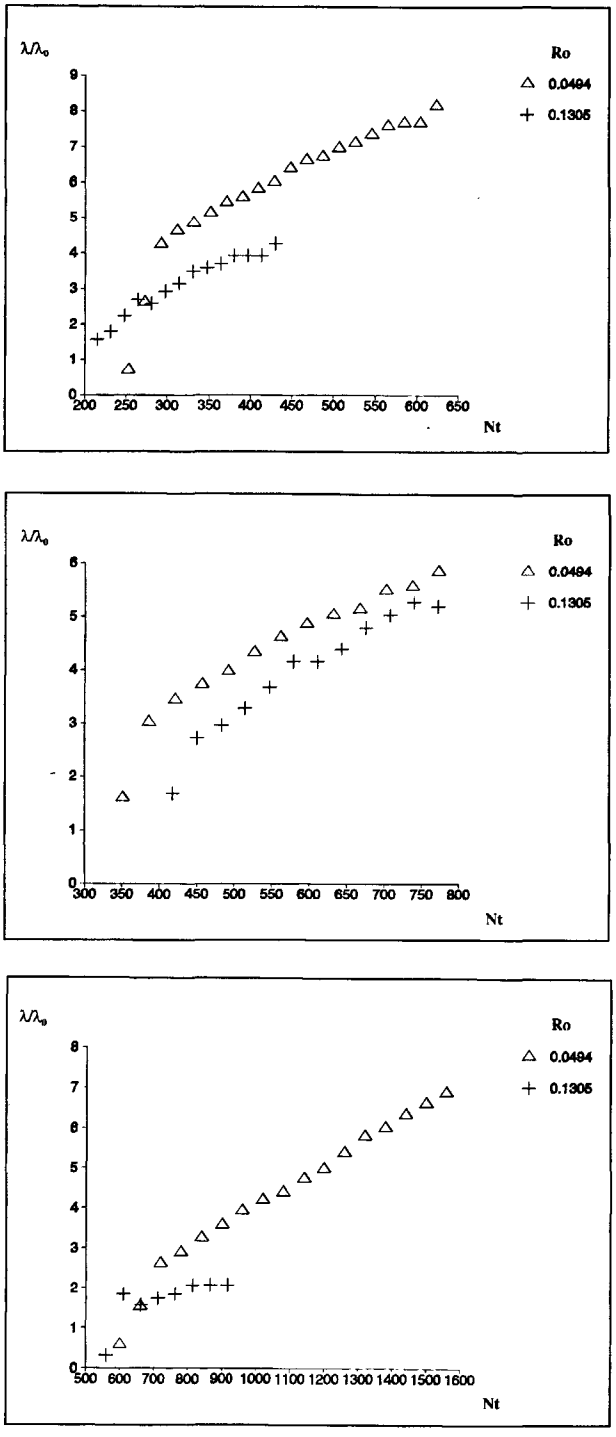

Figure 10

Dimensionless plots of boundary current width λ/λ_0 (see equation 5 b) at $x_0/R = \pi$ versus time Nt for $(\Delta\rho/\rho_0)$ = a) 0.002; b) 0.007; c) 0.0204 and Ro values shown.

measurement station x_0, so it was impossible to measure the width of the boundary current for this case. The results for Ro = 0.049 and 0.13 are given in the three graphs of Figure 10, each for fixed values for the fractional density difference $(\Delta\rho/\rho_0)$. The graphs show a clear increase in surface boundary current width with respect to time at the reference location, and the rate of increase with time is essentially constant. The width decreases with increasing Rossby number, all other factors fixed. Note that in all

Table 2

Summary of linear regression fits to current width-time growth curves (see text).

Ro	Slope	No. of observations
0.0494	1.13 ± 0.35	9
0.1305	1.28 ± 0.39	10

plots showing the variation of the boundary current width with time, there is an initial growth associated with the profile of the nose of the current as it passes the reference station. After the passage of the nose, the long term growth of the current width can be discerned.

Quantitative comparison with the viscous stage $t^{1/4}$ scaling outlined in the "Theoretical aspects" section may be attempted by plotting the width as a function of time on a logarithmic scale and applying a best fit regression line. Precautions have to be taken to ensure that the first or first two measurements made after the nose has just passed the reference station are not included in the regression analysis in order to eliminate influences of the shape of the nose of the current. It is noted further that the boundary current reaches and passes the reference station after an interval which is comparable to the empirically-determined viscous-dominated phase of the boundary current motion. Thus, there is a possibility that the viscous balance used to derive (8) may be weakened for some of the current width data points included in the analysis. The results of the analyses, for fixed Ro, are given in Table 2.

The values for the slope of the regression fit do not vary significantly with increasing Ro. Moreover, the results show relatively poor agreement with the viscous stage scaling prediction, which would result in a slope + 1/4 [*see* (8)].

By averaging the width at x_0 over each experiment (*i.e.* by measuring the mean width λ_m over the period taken by the boundary current to complete one circuit of the tank), a similar graph to Figure 9 may be compiled - *see* Figure 11,

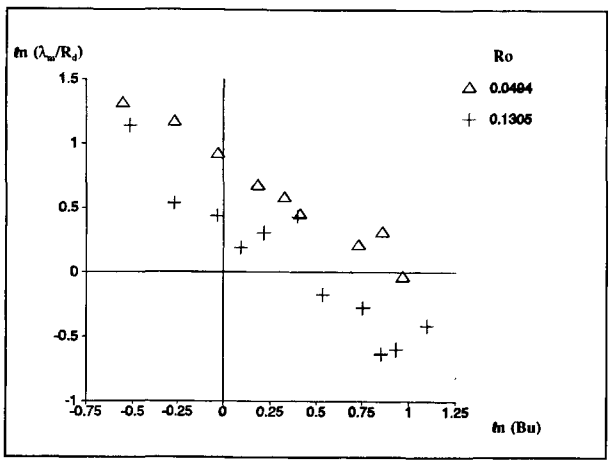

Figure 11

Dimensionless plot of mean boundary current width λ_m/R_d versus Bu for Ro values shown.

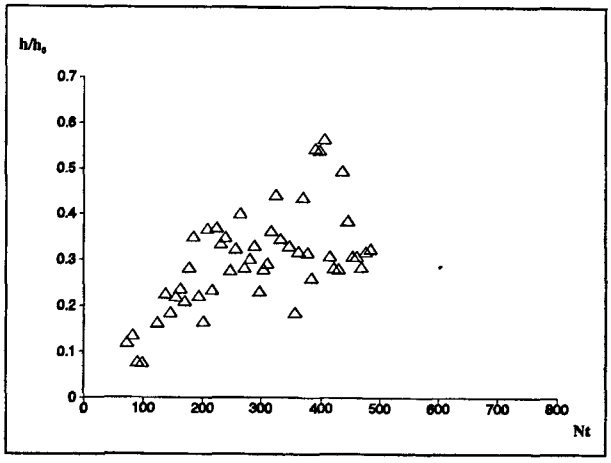

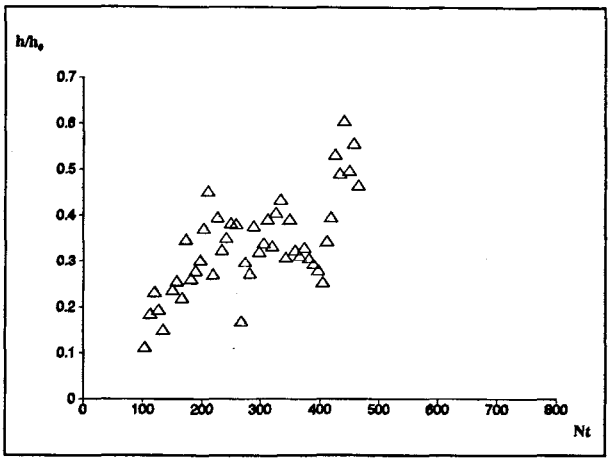

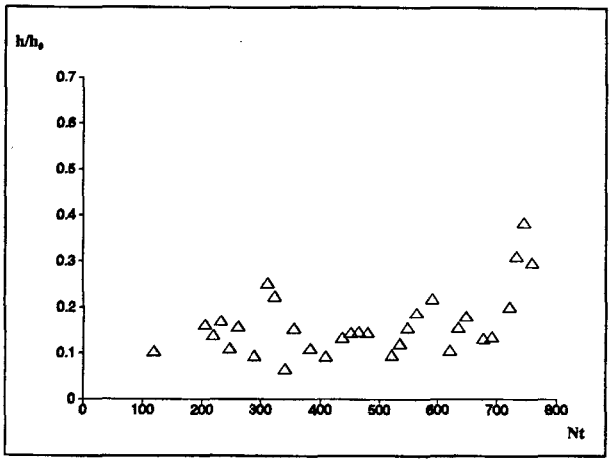

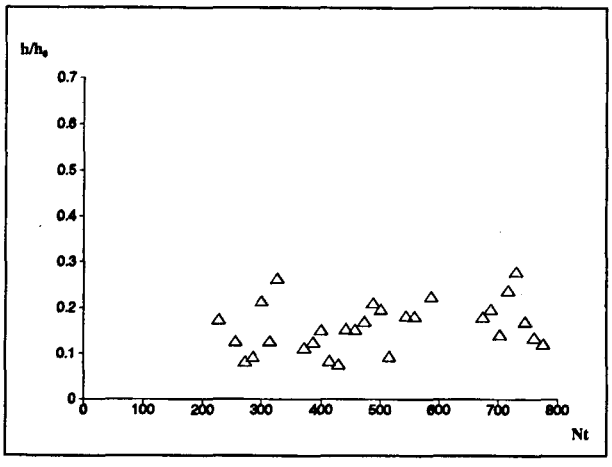

Figure 12

Dimensionless plots of boundary current depth h/h_0 (see equation 5 a) versus Nt for $x_0/R = \pi$, $y_0/R = 0.97$, [Ro:(Bu)(Fr): α: Ξ] = [0.125:0.0066:30:0.4:9.1] and [$(\Delta\rho/\rho_0)$] = (a),(b) 0.002 and (c),(d) 0.006.

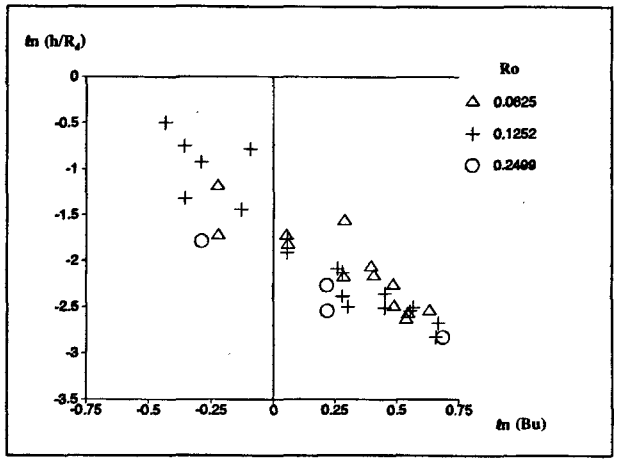

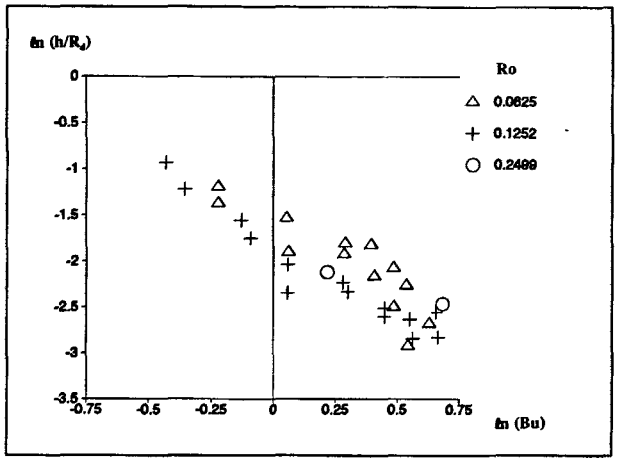

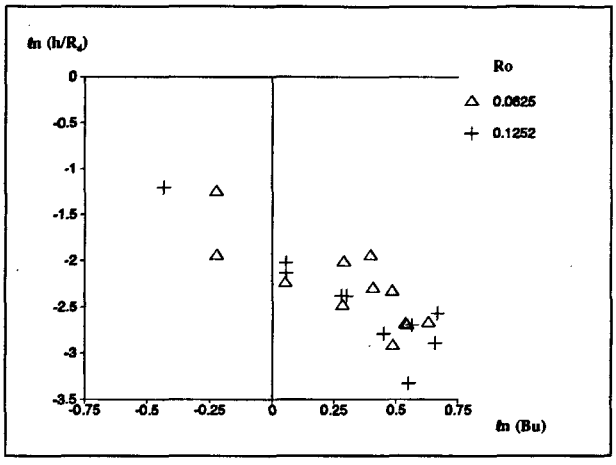

Figure 13

Dimensionless plot of mean boundary current depth h_m/R_d versus Bu for $x_0/R = \pi$, y_0/R = a) 0.97; b) 0.83; and c) 0.70, for (Bu)(Fr) = 0.009 and Ro values shown.

in which the mean width λ_m normalised by the Rossby radius R_d is plotted against Bu on a logarithmic scale. This plot shows a clear decline in averaged boundary current width for increasing Bu, with the rate of decline increasing with increasing Ro.

Boundary current depth

Here, the boundary current depth $h(x_0, y_0, t)$ at a given location (x_0, y_0) is scaled with the depth h_0 (*see* equation 5 *a*) and the results are presented as a function of dimensionless time Nt. Measurements were taken at $x_0/\pi R$ = 0.5, 0.67, 0.83 and 1.0, at three different radial positions y_0. However, evaluations for the probes in the experiments containing measurements sequences for all the six probes were generally not numerous enough to provide sufficient quantitative results for determining the time-dependent behaviour of the depth at each location. The results of these measurements are only used to calculate the mean depth per experiment.

The single probe experiments were carried out with probe 1 at $x_0/\pi R = 0.5$ and 0.83 at $y_0/R = 0.97$ from the centre of the tank, for two different values of the relative density difference $(\Delta\rho/\rho_0)$. Because the single probe was measuring continuously, a much greater number of data points was obtained than with the experiments with six probes. Only the results of the single probe experiments are presented here - *see* Figure 12.

The graphs show that the depth of the current at a fixed reference station increases with time, and that this increase is faster for lower relative density differences $(\Delta\rho/\rho_0)$. As with the nose velocity and the boundary current width data, averaged depths have been calculated for each experiment. For consistency, the values are scaled with the Rossby radius of deformation and plotted against the Burger number on a logarithmic scale (*see* Fig. 13). The values for the probes 1 + 4, 2 + 5 and 3 + 6, respectively, have been combined because the radial positions for these probes were the same. Figure 13 shows that the time-averaged depth of the boundary current decreases with increasing Bu, as was the case with the time-averaged width of the current. Changes in the value of the Rossby number have an insignificant effect on the principal dependence upon the Burger number. For given external conditions, the mean depth is seen to decrease as the radial position decreases (as measured from the centre of the tank), in consonance with the idealised structure of the flow shown in Figure 2.

Frontal instabilities

For those flows which were unstable, the distortions of the frontal interface could be followed over a number of frames in a given sequence and the amplitudes and radial growth rates could be calculated. Data showing the dependence of the time- and x- averaged amplitudes (normalised by R_d) upon Bu are shown in Figure 14. The general tendency shown by the plot is a decrease in normalised amplitude with increasing Bu, though the scatter precludes any delineation of a dependence upon Ro.

In some experiments, the pattern of instabilities was sufficiently regular that an associated wavelength could be measured. This was only possible for experiments with Ro = 0.049 or 0.246, as the patterns in the experiments with Ro = 0.13 showed insufficient regularity. Figure 15 shows the wavelength data as a plot of wavelength (normalised by R_d) *versus* Bu for the two values of Ro. The results show a decrease in wavelength for increasing Burger number and an indication of a stronger decrease for the lowest of the two Ro values.

SUMMARY AND DISCUSSION

The data presented in the previous section show a number of features which are of interest. For example, during the initial phase of motion of the boundary current the nose velocity is shown to decrease relatively smoothly with time in all cases. However, a stage is then reached when the smooth decay of the nose velocity with time is arrested; the velocity is then seen to fluctuate with time with significant and relatively sudden increases and decreases in magnitude (*see* below) being demonstrated. Attempts to apply simple scaling arguments to this initial stage are qualitatively successful, with the predicted long term decay in nose velocity due to frictional effects being illustrated clearly. With regard to quantitative comparisons with these scalings for the decay process, there is significant discrepancy between prediction and measurement. It seems clear that one reason for this discrepancy is the neglect of interfacial mixing in the theoretical model. As the probe data illustrate, there is evidence of considerable mixing at the lower interface of the current and this will of course serve to increase the nose velocity decay rate over that predicted by (7). Not least, it results in a reduction in the along-shore driving pressure gradient from the value $g(\Delta\rho)(h_0-h)/\rho_0 X$ adopted for the scaling. Likewise, the mixing would tend to increase the width of the boundary current over that of the unmixed case for a given time and reference station. The quantitative discrepancy in the width data confirm the validity of this hypothesis.

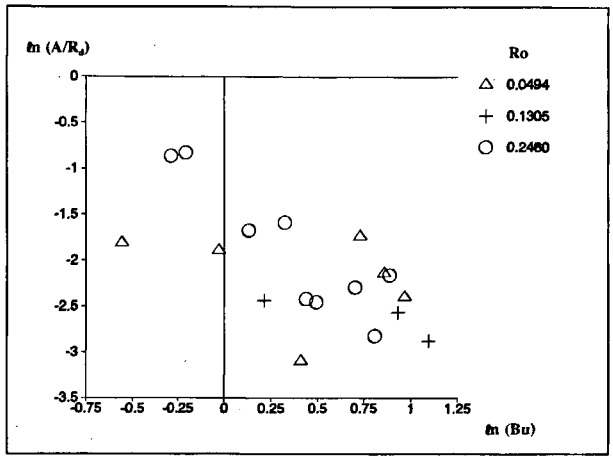

Figure 14

Dimensionless plot of mean amplitude A/R_d of instabilities versus Bu for Ro values shown.

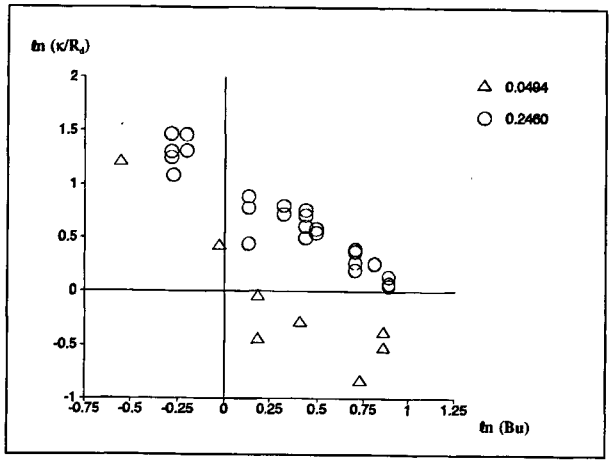

Figure 15

Dimensionless plot of mean wavelength κ/R_d *of instabilities* versus *Bu for Ro values shown.*

The interpretation of the data pertaining (*see* above) to the final stage of the motion in which there are large amplitude excursions in the nose velocity is less clear. Random errors in the nose velocity measurements are responsible for some uncertainty in the data, because of inadequacies in the flow recording system and the difficulties in locating unambiguously from the photographic negatives the nose and the lateral boundary of the current. It is also noted that some of the photographic negatives were not taken in phase with the modulation of the rotational speed of the system. The fluid in the tank (both the salt and the fresh water bodies) moved back and forth with respect to an observer fixed in a uniformly rotating frame, with an amplitude proportional to the amplitude of the modulation. However, since the timelapse between two photographs was not always equal to an integral number of modulation periods, shots were taken at different phase angles stages in this oscillatory interior motion. This lack of synchronisation can manifest itself as a sampling bias in the velocity-time plots, with the effect being stronger with higher values of the Rossby number. This is confirmed by plots where the decay profiles (*e.g.* for Ro = 0.246) show relatively more erratic behaviour at large times than for the lower Ro counterpart cases. The effect of the sampling bias is to indicate only the low frequency response behaviour, since the period between photographic exposures was significantly greater than the modulation period $2\pi/\omega$. It would be misleading therefore to interpolate linearly between successive data points on such plots, since this procedure would exclude high frequency fluctuations in the nose velocity.

An interesting feature can be seen in the decay profiles of Figures 6 and 8. In nearly all cases, the nose velocity shows an increase in value following a monotonic decay. Study of the negatives reveals that the increase in nose velocity is associated with the formation of a secondary separated front generated far downstream of the source (*see* section "General features of the flow field"). As indicated previously, this feature arose in twenty out of the thirty visualisation experiments, mainly in the experiments with the lower values of Ro. An illustration of the splitting of the boundary current and the subsequent different decay behaviours of the primary and secondary boundary currents is presented in Figure 16. It can be seen that the velocity of the nose of the original boundary current decreased continuously with time according to the predicted behaviour for a viscous friction model. The generation of the secondary boundary current results (*see* Fig. 16) initially in an increase in the nose velocity of the source material and it is this behaviour which is detected in the earlier Figures 6-8. As Figure 16 demonstrates, the initial increase in the velocity of the nose of the secondary feature is followed subsequently by a mean decrease with time, though the influence of the oscillatory crossflow distorts a simple monotonic decay.

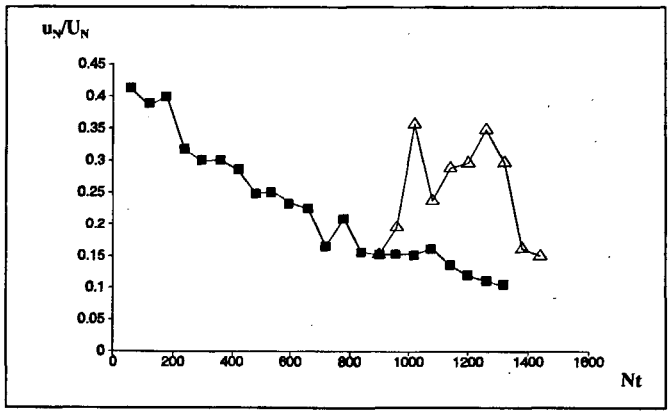

Figure 16

Dimensionless plot of normalised nose velocity u_N/U_N versus *time Nt showing splitting of boundary current into primary (■) and secondary (Δ) branches.*

It is useful to note that the splitting behaviour has been reported earlier by Stern *et al.* (1982) for a different though related flow configuration (a dam break discharge of buoyant fluid in a uniformly rotating fluid). Specifically, Stern *et al.* (1982) showed that any boundary current with a dimensionless width greater than 0.42 (scaled with R_d) must undergo bifurcation into a thin current which leaves the wide current behind, before it can propagate along the wall. This behaviour is independent of the value of potential vorticity and of the lower layer depth. Though it is tempting to explore the significance of these predictions for the present case, the different flow configurations for the two cases preclude more than a passing mention of the earlier study. Direct quantitative comparison between the two will be postponed to a later date when the potential vorticity distributions in the two cases can be measured and compared.

The results shown in Figures 6-8 confirm that the nose velocity is initially that $[g(\Delta\rho)(h_0)/\rho_0]^{1/2}$ of the inviscid geostrophic boundary current, at the onset of the boundary current flow. The subsequent decay with time of the nose velocity is qualitatively described well by a viscous friction model, but the results (*see* Tab. 1), obtained after averaging over the experiments with constant Ro, show that the decline is stronger than the expected $t^{-1/4}$

behaviour for higher values of Ro. This can be explained partially by the tendency of the nose of the boundary current to mix quickly with the tail at the higher values of Ro, and also by the deficiencies of a model which somewhat arbitrarily separates the current motion into three distinct stages. The viscous friction model for the intermediate time behaviour of the current presumes a constant rotational speed Ω_0. This approximation might be expected to describe well the low Ro cases, but it is clearly inadequate for cases in which the induced sloshing motions are significant. In the latter circumstances, interfacial and lateral mixing processes (*see* above) of the two fluid bodies are enhanced, thereby reducing the magnitude of the driving pressure gradient and increasing the decay rate of the nose velocity over the unmixed values. Even for the lowest values of Ro, the quantitative discrepancy between the measured and predicted decay in u_N with time confirm that the assumption of no interfacial mixing between the buoyant source fluid and the underlying receiving waters is inadequate. Mixing effects also explain the behaviour of the depth with respect to changes in the value of Bu (*see* Fig. 13). An increase in the relative density difference $(\Delta\rho)/\rho_0$ (and thus in Bu) causes an increase in the gravitational stability of the buoyancy current; this, in turn, results in reduced mixing. Consequently, the growth of the boundary current depth with time is less than for lower relative density difference counterpart cases, as shown in Figure 12 and in Table 3 below.

From this table it is clear that the growth rate of the depth of the boundary current with time decreases with increasing Bu.

Because the time of formation of the separated secondary front is essentially independent of Bu, but dependent on Ro, it is likely that it is formed due to the effects of the oscillating crossflow. The width of the secondary current is typically one order smaller than the width of the main boundary current (Jacobs, 1992). There are several mechanisms which might influence the formation of the secondary current in the laboratory system. Firstly, it is noted that the oscillatory crossflow is generated in the experiments by the oscillatory modulation in the rate of rotation of the container. Thus, the interior fluid is forced principally *via* motions generated in side wall boundary layers on the inner surfaces of the rotating container. For a non-rotating system, the two-dimensional oscillatory motion of a boundary is known to result in the formation of a Stokes boundary layer (Schlichting, 1955) having a velocity structure

$$u(y, t) = R(\Delta\Omega)e^{-\gamma} \cos(\omega t - \gamma) \qquad (9)$$

with $\gamma^2 = y^2\omega/2\nu$. This solution (valid for two-dimensional forcing and therefore unaffected by the background rotation Ω_0 of the system) indicates a dimensional oscillation boundary layer thickness of a few millimetres in the present experiments. For flows in a uniformly rotating system, side wall Stewartson boundary layers (*e.g.* Moore and Saffman, 1969) also form. The thickest of the two Stewartson layers has a width $\delta_{1/4}$ which is of order $E^{1/4}H_0$ (where E is the Ekman number of the flow), and for the present experiments represents a dimensional thickness of between

Table 3

Summary of linear regression analysis of variation in mean depth with time (see Fig. 12).

Bu	Slope	No. of observations
0.7485	0.64 ± 0.08	50
0.7002	0.58 ± 0.09	47
1.2971	0.32 ± 0.15	31
1.3234	0.31 ± 0.18	29

5 and 10 mm. Finally, it is known that the oscillatory motion of a vertical plate in a uniformly rotating homogeneous fluid can generate a horizontal rectified flow along the plate (Zhang *et al.*, 1993), because of the asymmetry in Ekman pumping between phases. This point is also relevant to the previous discussion on the Stokes layer in a rotating system, since the appropriate length scales to consider in these cases are $[\nu/(\omega \pm \Omega_0)]^{1/2}$ and not the scale $(\nu/\omega)^{1/2}$ appropriate for the non-rotating cases. The results of Zhang *et al.* (1993) indicate that a rectified boundary current of a few millimetres width is to be expected for the present case. Thus, all three mechanisms which operate in the present configuration give rise to side wall boundary layers which match well the scale of the boundary separation phenomenon described above. Unfortunately, the interaction and relative dominance of the three individual mechanisms (and their modification by centrifugal effects and the buoyancy of the boundary current) are presently unresolved. Likewise, in this regard, questions remain concerning the validity of the scaling for the friction terms in equations 2 *a-c*. Thus far, the scalings are based upon the premise that $\nu[\partial^2 u/\partial y^2] \sim \nu(\partial^2 u/\partial z^2) \sim \nu U/\lambda^2$ for the viscous stage [*see* equation (7)]; the existence of a smaller sidewall boundary length scale associated with the above mechanisms may cause the above scaling to be violated, with the result that the $t^{1/4}$ behaviour derived in the "Theoretical aspects" section requires modification (as indicated by the rather poor quantitative agreement seen in the "Quantitative results" section). Further investigations on the structure of the sidewall boundary are required before these questions are resolved.

Figure 14 reveals that the amplitude of the instabilities decreases with increasing Bu only for the experiments with Ro = 0.246. For the other experiments there is only a weak decline detectable. As discussed in an earlier section, the flow patterns of the experiments with the high value of Ro were distinctively different from the other experiments. With the assumption that the influence of baroclinic and barotropic instabilities is proportional to the ratio of the squares of the boundary current width and the Rossby radius R_d (Killworth *et al.*, 1984), it is clear from Figure 11 that for increasing Bu and Ro the baroclinic influences on the instability process have decreased. Therefore, it is likely that the instabilities formed in the experiments with Ro = 0.246 are barotropic in nature.

Figure 15 shows an explicit decrease in the wavelength of the instabilities with increasing Bu, and an increase with increasing Ro. The values are of the same order of

magnitude as predicted by the model of Killworth *et al.* (1984), the dimensionless values (scaled with R_d) being of the order 2-4. Griffiths and Linden (1982) found a dependence on the width of the current in two regimes; for wide currents (the width being greater than R_d) their experiments showed wavelengths that were constant multiples of R_d, while narrow currents (with a width smaller than R_d) showed wavelengths that were a constant multiple of the boundary current width. If these results are placed in the context of the present experiments, it is found that the wavelength is indeed a multiple constant of the boundary current width for the experiments with Ro = 0.246. For the latter case, the averaged value of the ratio of wavelength and boundary current width is equal to 2.13 ± 0.28, very close to the number 2.2 ± 0.3, given by Griffiths and Linden.

Finally, it is appropriate to make connections between the experimental model data and the Channel flows described in the introductory sections. The issue of the relative influence of the river plume salinity fronts and the tidal stirring fronts for the Channel situation remains a complex one, since there are doubts over the applicability of the shelf sea tidal stirring model to near shore situations affected by river outflows. In addition, the tidal stirring model in its original form does not incorporate effects due to either surface wind stress or background rotation. Recent extensions of the model to include these effects are presently underway (Simpson, personal communication). The river plume mechanism for coastal front formation has been considered in isolation in the present modelling investigation, and it is of interest to compare the model predictions with relevant field data. Adopting the prototype values presented in the "Physical system" section, it is relatively straightforward to estimate the values of U_N, h_0 and λ_0 from (1)-(8) as 0.1 m.s^{-1}, 5 m and 1 km respectively. Such scales for the nose velocity, current depth and current width respectively close to the river inlet accord well with field data where available, indicating that the scaling close to the source is satisfactory. The scalings also indicate reductions with distance from the inlet of between 5 and 8 in the nose velocity in a typical tidal cycle (Fig. 6-8) and a growth in boundary current width with t^{ψ} (with ψ approximately 1.2 - *see* Tab. 2) at a typical far-field along-shore station. At the same station the nose velocity shows a decrease with $t^{-\zeta}$ (with ζ being between 0.4 and 0.8). Thus far, field data are not yet available to test these far-field predictions of the model but the scales which emerge from the study seem to be in satisfactory agreement with values to be expected in the region in question.

Acknowledgements

The project reported here comprised part of the physical modelling component of the *Fluxmanche 1* investigation funded by the European Communities MAST 1 Programme, with supplementary EC support through the award of a one year postgraduate bursary award to PTGAJ. The authors acknowledge this support with gratitude and extend thanks for technical help from Eric Moser, Ernie Kuperus, and Fraser Smith. Neil Buirski and Graeme Ripley carried out a number of valuable preliminary experiments as part of their undergraduate projects and very useful discussions on the results of this investigation were held with Gabriel Chabert d'Hières, Simon Boxall, Martin Bohle-Carbonelle, John Simpson and Gert Jan van Heijst. Inspiring leadership of the project was given by Louis Cabioch, the Fluxmanche Project Coordinator. Additional travel support for aspects of the work was kindly provided by: a) The British Council UK-France Alliance programme; and b) NATO Scientific Affairs Division.

REFERENCES

Brylinski J.-M. and Y. Lagadeuc (1990). L'interface eaux côtières/eau du large dans le Pas-de-Calais (côte française): une zone frontale. *C. r. Acad. Sci., Paris*, **311**, 2, 535-540.

Chao S.-Y. (1988). River-forced estuarine plumes. *J. phys. Oceanogr.*, **18**, 72-88.

Davies P.A., H.J.S. Fernando, P. Besley and R.J. Simpson (1991). The generation and spreading of a turbulent mixed layer in a rotating stratified fluid. *J. geophys. Res.*, **96**, C7, 12567-12585.

Garvine R.W. (1981). Frontal jump conditions for models of shallow, buoyant surface layer hydrodynamics. *Tellus*, **33**, 301-312

Griffiths R.W. (1986). Gravity currents in rotating systems. *A. Rev. Fluid Mech.*, **18**, 59-89.

Griffiths R.W. and P.F. Linden (1982). Laboratory experiments on fronts. Part 1: Density driven boundary currents. *Geophys. astrophys. Fluid Dynam.*, **19**, 159-187.

Jacobs P.T.G.A. (1992). Dynamics and stability of buoyant fresh water boundary currents in tidal crossflows. *M. Sci. dissertation, Eindhoven University of Technology, Netherlands.*

Kao T. (1981). The dynamics of oceanic fronts. Part II: Shelf water structure due to freshwater discharge. *J. phys. Oceanogr.*, **11**, 1215-1223.

Killworth P.D., N. Paldor and M.E. Stern (1984). Wave propagation and growth on a surface front in a two-layer geostrophic current *J. mar. Res.*, **42**, 761-785.

Matthews A. and S.R. Boxall (1991). Airborne remote sensing of suspended sediment matter. *Fluxmanche, 1st Annual Progress Rept: Hydrodynamics and Biogeochemical Fluxes in the Eastern Channel; Fluxes into the North Sea*, 84-90.

Moore D.W. and P.G. Saffman (1969). The structure of free vertical shear layers in a rotating fluid and the motion produced by a slowly rising body. *Phil Trans. R. Soc.*, **A 264**, 597-634.

Pingree R.D. and D.K. Griffiths (1978). Tidal fronts on the shelf seas around the British isles. *J. geophys. Res.*, **83**, 4615-4622.

Schlichting H. (1955). *Boundary Layer Theory*. Pergamon Press Ltd, London, UK.

Simpson J.H. (1981). The shelf sea fronts: implications of their existence and behaviour. *Phil. Trans. R. Soc.*, **A302**, 531-546.

Simpson J.H. and I.D. James (1986). Coastal and estuarine fronts. in: Baroclinic Processes on Continental Shelves, C.N.K. Mooers, editor. American geophysical Union Monograph, Washington, D.C., *Coast. estuar. Sci. Series*, **3**, 63-94.

Stern M.E., J.A. Whitehead and B.L. Hua (1982). The intrusion of a density current along the coast of a rotating fluid. *J. Fluid Mech.*, **123**, 237-265.

Zhang X., D.L. Boyer, G. Chabert d'Hières, D. Aelbrecht and H. Didelle (1993). Rectified flow along a vertical coastline. *Dynam. Atmos. Oceans* (in press).